Development and Testing of an Advanced Hydrometeor-Phase Algorithm to Meet Emerging Needs in the Aviation Sector

HEATHER DAWN REEVES,[a,b] NATHAN LIS,[a,b] GUIFU ZHANG,[c] AND ANDREW A. ROSENOW[a,b]

[a] *Cooperative Institute for Mesoscale Meteorological Studies, University of Oklahoma, Norman, Oklahoma*
[b] *NOAA/National Severe Storms Laboratory, Norman, Oklahoma*
[c] *School of Meteorology, University of Oklahoma, Norman, Oklahoma*

ABSTRACT: New regulations are being issued by the Federal Aviation Administration (FAA) that require three-dimensional hydrometeor-phase diagnosis, including discrimination between freezing rain (FZRA) and freezing drizzle (FZDZ), for all commercial airports in the United States. Herein, a novel hydrometeor-phase algorithm, the spectral bin classifier (SBC), is adapted to meet these requirements. First, the SBC's particle size distribution (PSD) is upgraded to be variable rather than fixed. This, along with some changes to the logic, allows for drizzle (DZ)/FZDZ to be diagnosed. Second, the SBC is modified to provide a low-altitude (LA), aboveground diagnosis (SBC-LA). Last, necessary changes to account for resolution issues in NWP thermal profiles are presented. Adding a dynamic-PSD capability improves the probability of detection (POD) by about 12%, but adapting the algorithm to include DZ/FZDZ worsens the PODs. This is due to potentially errant reports of rain (RA)/FZRA in environments that are more conducive to DZ/FZDZ. Assuming a diagnosis of DZ is a hit when RA is observed, and likewise for FZRA/FZDZ, increases the POD by between 35% and 60%. Although performance statistics for SBC-LA cannot be computed, about one-third of all RA and DZ soundings herein have an elevated layer of FZRA/FZDZ, underscoring the importance of an aboveground diagnosis for the aviation sector. The comparatively low vertical resolution of NWP profiles is found to degrade the SBC's performance. Interpolating to a higher resolution helps to mitigate this problem. Several case studies of mixed phases at different airports are presented to highlight the enhanced decision support made possible by the above modifications.

KEYWORDS: Freeze events; Freezing precipitation; Icing; Algorithms; Classification; Forecasting techniques

1. Introduction

To prevent icing-related accidents, the Federal Aviation Administration (FAA) is implementing new standards that limit flight into and out of commercial airports during freezing precipitation. These guidelines require explicit discrimination between freezing drizzle (FZDZ) and freezing rain (FZRA) both at the surface and aloft (Cober and Isaac 2012; FAA 2015). Because the FAA uses a set particle-size threshold to discriminate between FZRA and FZDZ, these guidelines require the hydrometeor phase to be diagnosed across the particle-size distribution (PSD) *and* in three dimensions. The aim of this research is to add capabilities to a novel hydrometeor-phase algorithm that allow it to meet these emerging requirements.

The Weather Surveillance Radar—1988 Doppler (WSR-88D) network has three-dimensional coverage over most of the conterminous United States (CONUS) and, thus, seems like a reasonable fit to meet the above needs. Moreover, several hydrometeor-classification algorithms that can be used to infer icing have been developed for the WSR-88Ds (Park et al. 2009; Plummer et al. 2010; Hallowell et al. 2013; Serke et al. 2013; Thompson et al. 2014). While these algorithms have value, the majority of commercial airports in the CONUS have only limited WSR-88D coverage and, consequently, suffer from varying degrees of beam broadening and/or overshooting that prohibit radar-inferred icing from being uniformly beneficial (Giangrande et al. 2005; Ryzhkov et al. 2005; Ryzhkov 2007; Cho 2010; Reeves and Waters 2019).

An alternative to radar-inferred techniques is NWP-derived hydrometeor phase. Several algorithms have been developed for this purpose. These range from implicit techniques that infer the phase based on temperature and humidity profiles to explicit ones that use surface mixing ratios. Regardless of the method, the majority of existing techniques have one or more limitations, such as assuming a single hydrometeor size (or using bulk microphysics), only providing a diagnosis at the surface, and/or only accounting for complete melting or refreezing—partial melting and refreezing are usually ignored (Ramer 1993; Bourgouin 2000; Manikin et al. 2004; Manikin 2005; Ikeda et al. 2013; Benjamin et al. 2016). Such assumptions make these algorithms unsuitable for meeting the FAA requirements and lead to unreliable performance in near-$0°$C environments (Bourgouin 2000; Manikin et al. 2004; Manikin 2005; Wandishin et al. 2005; Ikeda et al. 2013; Reeves et al. 2014; Elmore et al. 2015).

A new algorithm for diagnosing the hydrometeor phase, the spectral bin classifier (SBC), has recently been introduced (Reeves et al. 2016, hereinafter RRK2016). The SBC is a one-dimensional bin-microphysics model that uses thermodynamic profiles to explicitly compute the liquid-water fraction (LWF) of individual hydrometeors as they descend from the top of the cloud to the ground. This approach results in a more accurate diagnosis, particularly for FZRA and ice pellets (PL), whose probabilities of detection (POD; i.e., the hit rate)

Corresponding author: Heather Reeves, heather.reeves@noaa.gov

are between 14% and 35% higher than existing operational algorithms (RRK2016). However, some modifications to the SBC are necessary for it to fully meet the FAA requirements. Chief among these is to graduate from using a climatological PSD to a dynamic one that varies in time and space. This may be accomplished through use of radar-derived PSD-extraction techniques, as several investigators have recently demonstrated (e.g., Zhang et al. 2006, 2008; Bukovčić et al. 2018, 2020; Mahale et al. 2019). Two other advancements are also necessary: Methods to diagnose the hydrometeor phase above ground as well as to discriminate FZDZ and drizzle (DZ) must be devised, and the algorithm has to be applied to NWP thermodynamic profiles rather than to observed soundings, because the latter lack sufficient temporal and spatial resolution. The goal of this research is to advance the SBC in these ways and to describe their effects on the algorithm's output.

This paper is organized as follows: Section 2 presents modifications made to allow for a dynamic PSD. Section 3 presents the inclusion of DZ categories and an aboveground diagnosis. Section 4 discusses the implications for transition to NWP input and shows some case-study demonstrations. Concluding thoughts are provided in section 5.

2. Advancing the SBC to include a dynamic PSD

a. SBC overview

We start with a cursory overview of the SBC. As noted above, it is a one-dimensional bin-microphysics model. Its inputs include the vertical profiles of temperature, humidity, and pressure.

A starting hydrometeor phase is declared at the top of the precipitation-generation layer, which is determined using relative humidity and wet-bulb temperature T_w. All hydrometeors across the PSD are then allowed to fall at a terminal velocity consistent with their size, phase, and degree of riming (if frozen). As they encounter melting and/or refreezing layers, their LWF is computed using equations for melting and refreezing from Trömel et al. (2014) and Kumjian et al. (2012). These are explicit computations that account for hydrometeor size, amount of riming, and terminal velocity and, additionally, allow for partial melting and refreezing of individual hydrometeors. Although the phase at the top of the profile is assumed to be the same across the size distribution, explicit treatment of each size bin can result in different phases within individual layers as hydrometeors fall.

The surface diagnosis is based on the integrated LWF at the bottom of the profile, the surface T_w, and whether there exists an elevated warm layer. Profiles with LWF greater than 85% are diagnosed as either rain (RA) or FZRA, based on the surface T_w (FZRA is declared when T_w is less than or equal to 0°C). Profiles with LWF less than 15% are diagnosed as snow (SN) or PL, differentiated by the presence of an elevated warm layer. RASN, RAPL, and FZRAPL mixes are diagnosed for LWFs between 15% and 85%, again differentiated by the surface T_w (as described above) and the presence of an elevated warm layer. SN and FZRA are also diagnosed

for completely subfreezing profiles. Their discrimination is based on whether T_w at the precipitation-generation layer is above or below a prescribed ice-nucleation temperature T_{ice}.

It is possible to vary the degree of riming in the SBC using a scaling between 1 and 5. A higher riming factor results in slower melting and faster terminal velocities. RRK2016 found that the best agreement to observations occurs for a riming factor of 1 (i.e., pristine crystals), hence, that value is used throughout this paper. The reader is referred to RRK2016 for a more in-depth description on the SBC's method and preliminary performance statistics.

b. Assessment of characteristic reflectivity for winter precipitation

RRK2016 tested six different PSDs from climatological disdrometer observations in central Oklahoma (see their Fig. 3). These PSDs were created by taking the mean of all PSDs from set reflectivity Z_H ranges. [The Z_H was determined from the lowest (or base) tilt from the nearest WSR-88D (Schuur et al. 2005).] The SBC produced the highest PODs when the PSD associated with Z_H between 20 and 30 dBZ was used. This was the lowest available range in their dataset.

The authors have anecdotally observed that 20–30 dBZ is a high range for winter storms and question whether the PSD advocated in RRK2016 is representative of the reflectivity in most near-0°C environments. We now evaluate this more precisely by comparing the surface precipitation type and intensity from Automated Surface Observing Station (ASOS; NOAA 1998) observations with Z_H. Ten-minute reports of FZRA and PL and 1-h observations of RA and SN are collected during winter seasons (October–March) from 1997 to 2020 across the CONUS. Observations that include hail are removed. The 10-min cadence for FZRA/PL ensures that new radar data have been collected for consecutive ASOS observations and the 1-h cadence for RA/SN keeps the number of these observations to a reasonable limit. This analysis is restricted to observations whose 2-m temperatures are between −10° and 5°C—the range in which icing is most prone to occur in the lowest 12 000 ft (3658 m) AGL [i.e., the top of the terminal air space (TAS); Bernstein 2000; Bernstein et al. 2005]. Sites reporting mixes and observations of "unknown" are discarded so that Z_H as a function of hydrometeor phase/intensity can be unambiguously determined. The Z_H used herein is from the range gate immediately above the ASOS and from the lowest (or base) tilt of the nearest WSR-88D to each ASOS. Sites reporting no echo are discarded. Some reflectivities are unreasonably high or low for the reported precipitation type or intensity. This is corrected by discarding observations whose reflectivity is in the 1st or 99th percentile for that category/intensity. There are 438 669 observations after all of the above exclusions are applied.

This analysis suggests that using a single PSD to represent all events is ill posed because Z_H has a broad range (from −19.5 to 43.5 dBZ; Fig. 1a). In addition, it indicates that the climatological PSD recommended by RRK2016 is not suitable in most near-0°C environments because only 22% of the observations are between 20 and 30 dBZ. The medians for
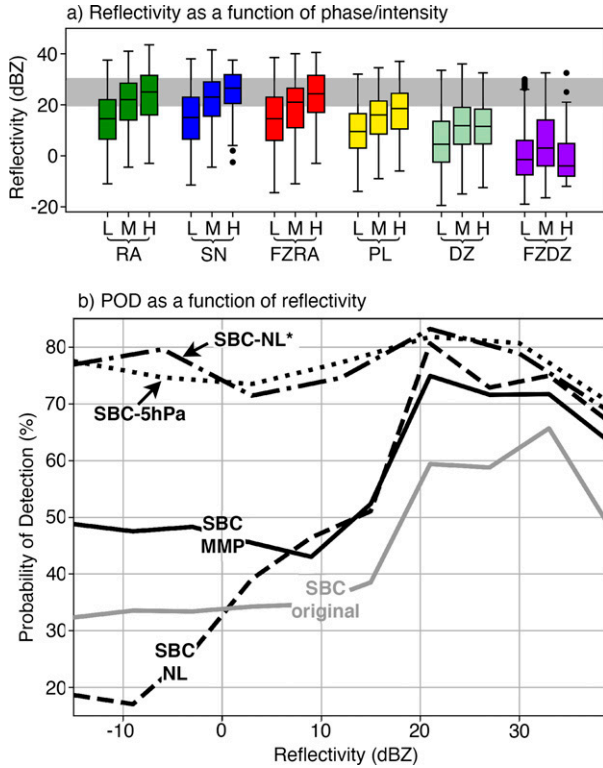
FIG. 1. (a) Reflectivity distributions for the different hydrometeor phases/intensities, and (b) POD for different iterations of the SBC. In (a), L, M, and H stand for light, moderate, and heavy intensity, and the gray shading indicates the 20–30-dBZ layer.

most categories/intensities are less than 20 dBZ. For some categories/intensities (light PL and all DZ/FZDZ), even the 75th percentile is less than 20 dBZ.

To evaluate the efficacy of the SBC as presented in RRK2016, observed precipitating soundings that correspond to augmented observations from the above dataset are used to initialize the SBC. Augmented observations are those where a human observer was present to correct misdiagnoses by the instrumentation. Herein, a corresponding sounding is defined as one that is within 35 km of the ASOS, as in Ramer (1993) and Reeves et al. (2014), and that is launched at the time of the observation. Completely subfreezing soundings are excluded as the SBC does not compute the LWF for this profile type, but rather automatically classifies them as described above. Mixes of RASN, RAPL, and FZRAPL are included in this analysis because these can be diagnosed by the SBC. There are 4416 soundings that meet the above criteria. This output is referred to as SBC-original (Table 1). In this and all subsequent experiments, a bin size of 0.1 mm is used.

Diagnoses from SBC-original are validated against ASOS observations as in Reeves et al. (2014), and the PODs and false alarm rates (FARs) are presented as a function of the observed precipitation type in Table 2. SBC-original shows similar trends to those reported in RRK2016. Namely, RA has a high POD, while FZRA and PL have lower PODs.

FARs are less than 10% for all categories. (The number of mixes is too few to provide robust statistics and, so, these are excluded from Table 2). The exact statistics obtained herein are different from RRK2016 because this dataset covers a different time period and is restricted to only the near-0°C environment. RRK2016 also used a quality-controlled set of soundings. This was not done herein in order to gain a fuller appreciation of the performance of the algorithm as it applies to real-time decision support (Reeves 2016). Hence, different PODs are expectable (Reeves 2016).

Evaluating the POD as a function of Z_H reveals some interesting behavior. The POD is comparatively high (between 54% and 61%) for soundings whose Z_H is between 20 and 35 dBZ (Fig. 1b). Observations whose Z_H is less than 15 dBZ have significantly lower PODs (less than 40%). Inspection of errant diagnoses for low-Z_H soundings shows that the majority of these (75%) have surface reports of SN but are diagnosed as either RA or FZRA. In every such instance elevated melting layers are present, which usually indicate RA or FZRA, consistent with the SBC output. This disagreement could be caused by several things such as radiosonde drift (Seidel et al. 2011), secondary ice production (Lauber et al. 2018; Phillips et al. 2018), or biases in the ASOS instrumentation that are not corrected by the human observers (NOAA 1998). Since the prospective causes for this bias are outside the scope of this research, we leave investigation of this interesting finding to future efforts.

c. The dynamic PSD method and resulting distributions

A dynamic PSD (i.e., one that varies in time and space) representative of the environment may allow for a more robust phase diagnosis via a more accurate size distribution [$N(D)$] and maximum particle size (D_{max}) as the SBC's LWF is functionally dependent on both (RRK2016). Herein, a modified Marshall–Palmer (MMP; Marshall and Palmer 1948; Table 1) PSD derived from the base Z_H is used and is assumed to be unchanged between the base tilt and the ground. This approach allows one to use CONUS-wide Z_H mosaics as input, thus minimizing the computational footprint—an important consideration for real-time implementation—while allowing for more advanced methods, such as those that exploit dual-polarized observations (e.g., Bukovčić et al. 2018; 2020; Mahale 2019) to be substituted as the science and technology mature. The SBC with this capability is referred to as SBC-MMP (Table 1).

SBC-MMP expresses $N(D)$ as

$$N(D) = N_0 \exp(-\Lambda D), \tag{1}$$

where D is the particle diameter, N_0 is the intercept parameter, and Λ is the slope parameter. The differing Z_H in SN versus RA is accounted for by scaling Λ, where

$$\Lambda = \begin{cases} \left(\dfrac{720 \times N_0}{Z_h}\right)^{1/7} & \text{if } H[Z_h] < \text{melting layer top} \\ 1.24 \times \left(\dfrac{720 \times N_0}{Z_h}\right)^{1/7} & \text{otherwise.} \end{cases} \tag{2}$$

TABLE 1. A list of the experiments included in this paper, the choice of PSD, the logic used to designate the phase, and whether the phase diagnosis is at the surface or aloft. SBC-25hPa and SBC-5hPa are denoted as being able to use either approach.

Expt name	Brief description	PSD	Logic	Phase diagnosis
SBC-original	Original version	Climatological	Integrated LWF	Surface
SBC-MMP	Modified MP	MP	Integrated LWF	Surface
SBC-NL	New logic	MP	Bin by bin	Both
SBC-LA	Low altitude	MP	Bin by bin	Aloft
SBC-25hPa	Interpolated to 25 hPa	MP	Bin by bin	Both
SBC-5hPa	Interpolated to 5 hPa	MP	Bin by bin	Both
SBC-final	MP, NL, and 5 hPa	MP	Bin by bin	Surface

In (2), Z_h is the measured reflectivity [$Z_H = 10\log(Z_h)$] and $H[Z_h]$ is the altitude of the midpoint of the radar beam. If $H[Z_h]$ is above the top of the melting layer (determined using the altitude of the 0°C isotherm from the environmental temperature profile), the phase at the beam's altitude is assumed to be SN and the 1.24 scalar is applied. The effect of the scalar is to steepen the slope resulting in a smaller D_{max} for the same Z_H in SN relative to RA. The constant of 1.24 is derived assuming the density of solid ice (1 g cm^{-3}) and is not strictly true for all ice particles (Zhang 2017), but its use here lays the necessary foundation for more advanced methods later on. The base tilt is above the melting-layer top in 38% of the soundings.

Intercept parameter N_0 is conditionally dependent upon Z_H as follows:

$$N_0 = \begin{cases} 8000 \times 10^{[(Z_{Hth}-Z_H)/10]} & (Z_H < Z_{Hth}), \\ 8000 & (Z_H \geq Z_{Hth}), \end{cases} \quad (3)$$

where the units for N_0 are m^{-3} mm^{-1}. The conditional N_0 in (3) allows for a higher concentration of small particles in light precipitation—a feature that has been observed in winter precipitation by other investigators (Waldvogel 1974; Thompson et al. 2004; Cao et al. 2006; Zhang et al. 2008). The Z_{Hth} is a threshold used to separate light

precipitation from moderate or heavy precipitation and is set to 9 dBZ, the median Z_H for all light RA, SN, FZRA, and PL and all intensities of DZ and FZDZ combined (Fig. 1a). A minimum $N(D)$ of 10^{-3} m^{-3} mm^{-1} is also imposed to be consistent with previous observations (Cao et al. 2006; Zhang et al. 2008).

Example PSDs for select Z_H (assuming a liquid phase) relative to SBC-original are provided in Fig. 2a. These compare favorably to observations and empirically derived equations made by previous investigators (e.g., Gunn and Marshall 1958; Sekhon and Srivastava 1970; Thompson et al. 2004) but have some considerable departures from SBC-original. The climatological PSD has a gamma-type distribution with a subtle decrease in $N(D)$ for hydrometeors less than 0.8 mm, as opposed to the high concentrations of very small particles in SBC-MMP. It is possible the climatological PSD is contaminated by sampling errors of the disdrometer (Cao et al. 2008), but note also that SBC-original is based on mostly RA observations collected during the warm season (Schuur et al. 2005) and so may not be representative winter PSDs.

d. Effects of a dynamic PSD on the hydrometeor-phase diagnosis

To illustrate the effects of changing the PSD on rates of melting and refreezing, the observed sounding/Z_H pairs described above are applied to SBC-MMP and compared with the output from SBC-original. SBC-MMP generally produces higher surface LWFs for Z_H less than 20 dBZ, with differences becoming more pronounced as Z_H is decreased (Fig. 2b). This is due to SBC-MMP's higher concentration of smaller droplets, which melt more rapidly than larger ones. There are relatively few observations of Z_H greater than 30 dBZ, but SBC-MMP produces similar LWFs to SBC-original at these intensities. This is due to the competing effects of a larger D_{max} relative to the large concentration of small particles.

Different LWFs only translate to a different diagnosis when one version of the SBC crosses a prescribed threshold while the other does not. This happens only rarely for RA, RASN, and FZRA. These profiles have rates of agreement between the two SBCs of 99%, 96%, and 100% (Table 3). Profiles with partial refreezing have less agreement. PL, FZRAPL, and RAPL have rates of agreement ranging from 35% to 78%. Because of its typically higher LWF, SBC-MMP diagnoses the majority of these profiles as a warmer phase (e.g., 53% of

TABLE 2. The POD (%) and FAR (%) binned according to the observed precipitation type for each of the experiments considered herein; "NA" indicates that phase is not declared using that version of the SBC.

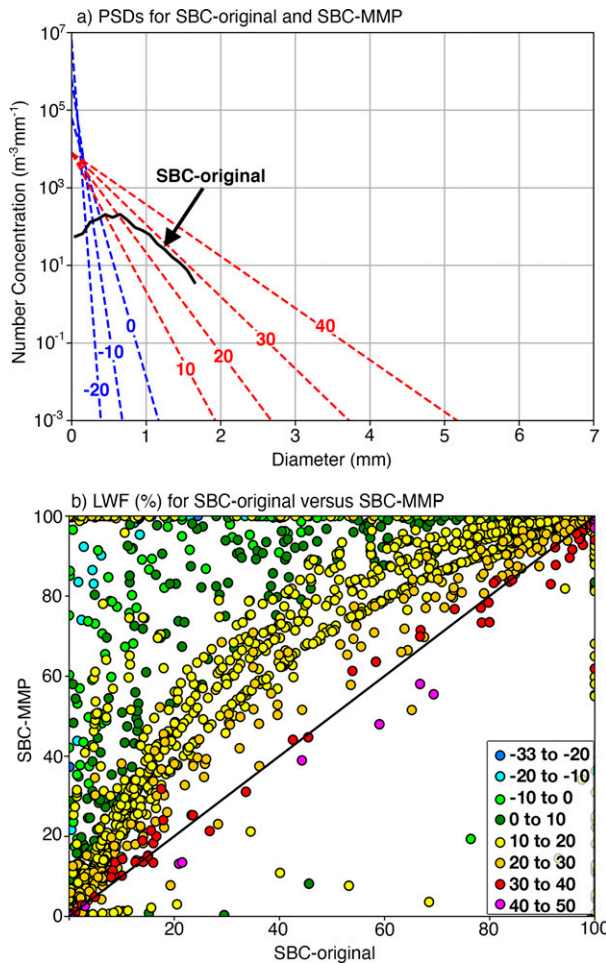|	RA	DZ	FZRA	FZDZ	PL
POD					
SBC-original	92	NA	52	NA	64
SBC-MMP	92	NA	60	NA	68
SBC-NL	89	39	55	44	68
SBC-NL*	93	NA	65	NA	68
SBC-25hPa	97	NA	55	NA	61
SBC-5hPa	94	NA	58	NA	64
FAR					
SBC-original	10	NA	7	NA	7
SBC-MMP	8	NA	6	NA	4
SBC-NL	2	4	5	1	3
SBC-NL*	2	NA	3	NA	3
SBC-25hPa	39	NA	8	NA	5
SBC-5hPa	22	NA	6	NA	5

FIG. 2. The (a) PSDs for SBC-original (solid curve) and for select Z_H in SBC-MMP [dashed curves, annotations indicate Z_H (dBZ) used for each curve], and (b) scatterplot of LWF for SBC-original and SBC-MMP. Output in (b) is color coded according to the observed Z_H (dBZ) as indicated in the inset.

TABLE 3. The distribution (%) of SBC-MMP diagnoses for soundings classified as RA, RASN, etc. by SBC-original (i.e., 99% of soundings diagnosed as RA by SBC-original are also diagnosed as RA by SBC-MMP and 1% are diagnosed as RASN). Values given in boldface show the rate of agreement (%) between the two versions of the SBC.

	SBC-original					
	RA	RASN	FZRA	PL	FZRAPL	RAPL
SBC-MMP:						
RA	**99**	4	0	1	0	60
RASN	1	**96**	0	0	0	0
FZRA	0	0	**100**	2	53	0
PL	0	0	0	**78**	12	1
FZRAPL	0	0	0	19	**35**	0
RAPL	0	0	0	0	0	**39**

two SBCs produce different LWFs at the surface (see insets in Figs. 3b,c,g,h). At Upton, the LWF in SBC-original is slightly larger than SBC-MMP, owing to its smaller D_{max} (Figs. 3d,e), but the disparity is sufficient to cause different diagnoses (FZRA vs FZRAPL). At Gray, the opposite occurs. The different LWFs result in a diagnosis of PL in SBC-original and FZRAPL by SBC-MMP. In this case, differences are due to the higher concentration of small particles in SBC-MMP (Figs. 3i,j). In either example, surrounding observations suggest a mix of FZRA and PL, in agreement with SBC-MMP (not shown).

The POD and FAR as a function of the observed precipitation type show an improved performance for both FZRA and PL by SBC-MMP (Table 2). The POD evaluated as a function of Z_H shows that SBC-MMP also preferentially performs better for Z_H greater than about 20 dBZ and somewhat poorer for low Z_H (Fig. 1b). Nevertheless, it routinely provides a more robust diagnosis than SBC-original for all Z_H ranges, with an average increase to the POD of about 12%. This is entirely due to the dynamic PSD in SBC-MMP as the algorithms are otherwise identical. This represents a roughly 50% increase relative to the improved performance of SBC-original as compared with other algorithms (RRK2016). SBC-MMP is used for baseline comparison of additional modifications in the remainder of this paper.

soundings diagnosed as FZRAPL by SBC-original are diagnosed as FZRA by SBC-MMP). Yet, colder diagnoses sometimes happen: 12% of the FZRAPL soundings from SBC-original are diagnosed as PL by SBC-MMP.

Examples where SBC-original and SBC-MMP produce different diagnoses occur at Upton, New York, at 0000 UTC 9 January 2018 (Figs. 3a–e) and Gray, Maine, at 1200 UTC 24 November 2019 (Figs. 3f–j). These soundings are similar in that they both have very-shallow elevated warm layers (Figs. 3a,f) that result in complete melting of smaller particles and only partial melting of larger particles in either version of the SBC (Figs. 3b,c,g,h). Both soundings also have surface-based subfreezing layers with a minimum T_w that is greater than T_{ice}. This results in no refreezing of particles that are completely melted but does allow for partially melted hydrometeors to refreeze before reaching the ground. Though both SBCs produce a combination of pure liquid and pure ice at the surface for both soundings, the

3. Adding capability to diagnose DZ and aboveground phases

a. Capability to discriminate FZDZ and DZ

An important capability for the FAA is the discrimination of FZDZ from FZRA. Using the integrated LWF across the entire PSD does not allow for this, but the same logic can be applied to the LWF in individual bins thus allowing FZDZ to be discriminated from FZRA by bin size. Herein, a bin size of 0.5 mm is used to match criteria issued by the FAA (FAA 2009). This new version of the SBC is referred as SBC-NL (new logic; Table 1). In SBC-NL, a phase is assumed to exist if it composes at least 1% of the total water content or if its integrated N(D) exceeds 10^2 m^{-3}. These thresholds are
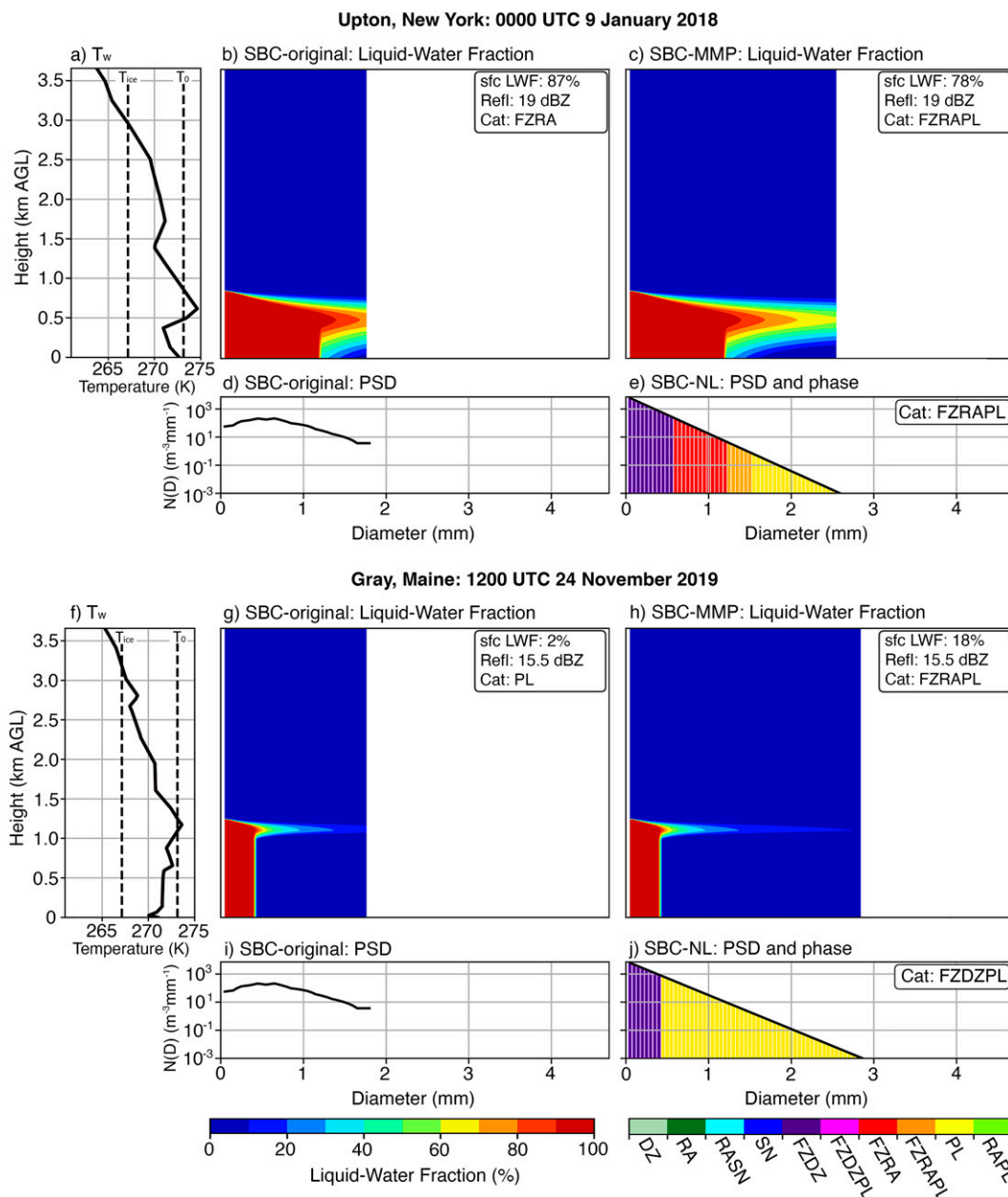
FIG. 3. (a),(f) The T_w profiles; the LWF diagnosis from (b),(g) SBC-original and (c),(h) SBC-MMP; the PSD from (d),(i) SBC-original and (e),(j) SBC-MMP—(e) and (j) also include the bin-by-bin surface phase diagnosis from SBC-NL. Other relevant diagnostics are included in the insets (sfc LWF refers to the integrated LWF at the surface). The times and locations of the various analyses are indicated in the figure.

chosen through trial-and-error and result in the highest PODs. SBC-NL is capable of diagnosing DZ and FZDZ in addition to several mixes, namely, DZSN, DZPL, and FZDZPL. These mixes are the drizzle equivalent to mixes already diagnosed by SBC-original and use the same rules as described in section 2a. In cases where both FZDZ and FZRA are diagnosed, the classification is simplified to only FZRA since flight restrictions associated with FZDZ are a subset of those imposed for

FZRA. The same declaration is made for DZ and RA. SBC-NL is otherwise identical to SBC-MMP.

Examples of SBC-NL output for the Upton and Gray soundings are provided in Figs. 3e,j. The diagnosis at Upton does not change as SBC-NL also diagnosis both FZRA and PL (Fig. 3e). At Gray, SBC-NL diagnosis FZDZPL (Fig. 3j), as opposed to the FZRAPL diagnosis made by SBC-MMP. While the distinction between FZRAPL and FZDZPL has historically been

TABLE 4. As in Table 3, but comparing SBC-MMP with SBC-NL.

	SBC-MMP					
	RA	RASN	FZRA	PL	FZRAPL	RAPL
SBC-NL:						
RA	**82**	0	0	0	0	0
DZ	10	0	0	0	0	0
RASN	6	**82**	0	0	0	0
DZSN	1	17	0	0	0	0
FZRA	0	0	**82**	0	0	0
FZDZ	0	0	10	0	0	0
PL	0	0	0	**84**	0	0
FZRAPL	0	0	7	1	**49**	0
FZDZPL	0	0	1	8	51	0
RAPL	1	1	0	1	0	**75**
DZPL	0	0	0	6	0	25

treated as more of an academic interest, the new certification rules of the FAA elevate this to a practical need.

The output from SBC-NL is compared with SBC-MMP in Table 4. As is expected, a fraction of all RA, RA-mix, FZRA, and FZRA-mix soundings are classified as their DZ counterparts by SBC-NL. There are also some cases where using the new logic teases out hydrometeor phases that are excluded when using the integrated LWF. For example, 8% of the PL soundings are diagnosed as FZDZPL, which may result in different decisions to protect aviation safety.

The PODs and FARs from SBC-NL are included in Table 2. The FAR slightly improves but both RA and FZRA have decreased PODs relative to SBC-MMP and quite low PODs for DZ and FZDZ. These decreased PODs occur predominantly in low-Z_H environments (Fig. 1b). Errant diagnoses in this range are mostly cases where RA is observed and DZ is diagnosed. It is not unreasonable to assume that reports of RA in such weak echo are wrong—that the precipitation phase is more accurately characterized as DZ (e.g., Heymsfield et al. 2002, 2010)—echo less than 5 dBZ suggests a maximum particle size that is too small to be classified as RA. Previous evaluations of precipitation-type algorithms have treated diagnoses of RA as a hit if DZ is observed and likewise for FZRA and FZDZ. Herein, we make a similar assumption and additionally assume a diagnosis of DZ is correct if RA is observed (and likewise for FZRA/FZDZ). This output is referred to as SBC-NL*. Doing this
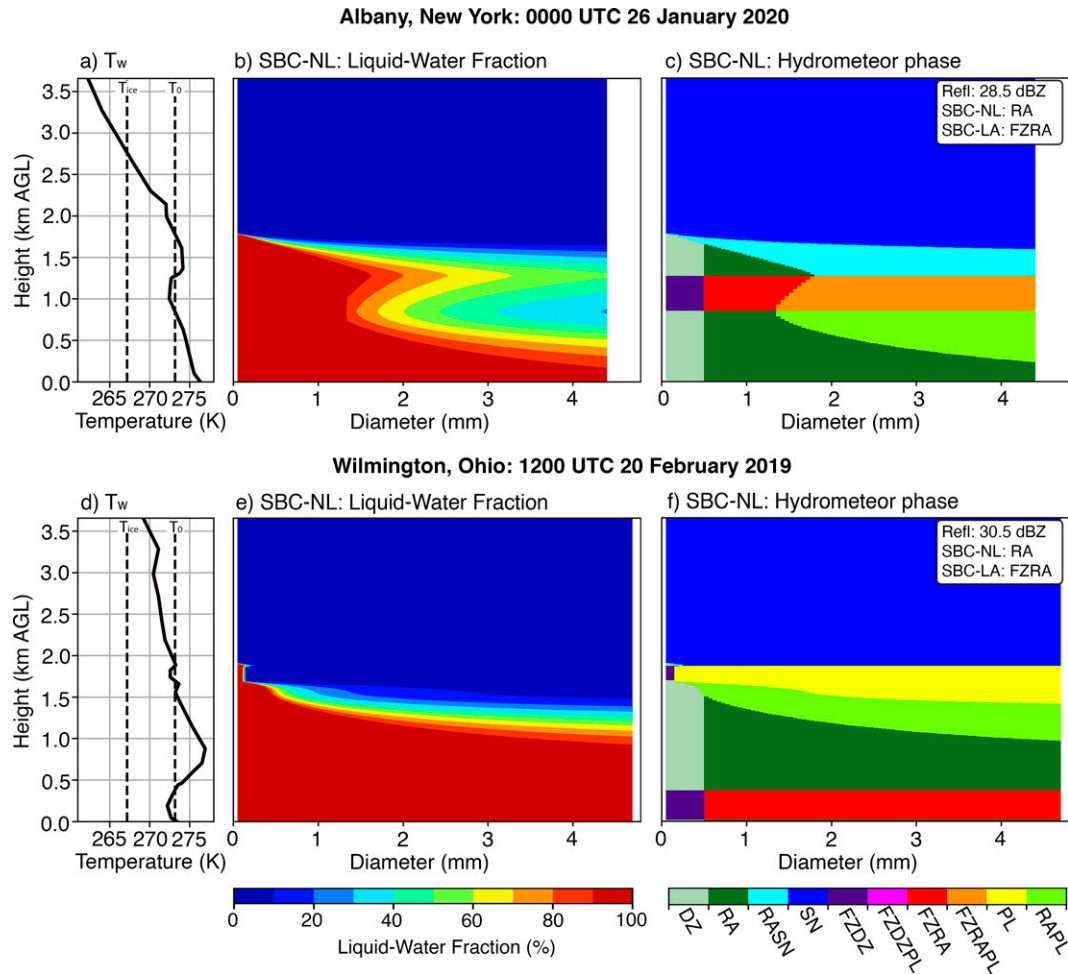

FIG. 4. (a),(d) The T_w profiles, and SBC-NL diagnoses of (b),(e) LWF and (c),(f) hydrometeor phase for the times and locations indicated in the figure. Relevant diagnostics are included in the inset.

TABLE 5. As in Table 3, but comparing SBC-NL with SBC-LA. In this comparison the surface observations from SBC-NL are compared with the most hazardous phase in the lowest 12 000 ft from SBC-NL (this output is referred to as SBC-LA).

	SBC-NL											
	SN	RA	DZ	FZRA	FZDZ	PL	RASN	DZSN	FZRAPL	FZDZPL	RAPL	DZPL
SBC-LA:												
SN	**100**	65	66	0	0	0	100	100	0	0	0	0
RA	0	**0**	0	0	0	0	0	0	0	0	0	0
DZ	0	0	**0**	0	0	0	0	0	0	0	0	0
FZRA	0	30	0	**100**	0	66	0	0	94	35	61	34
FZDZ	0	5	34	0	**100**	32	0	0	6	65	31	63
PL	0	0	0	0	0	**2**	0	0	0	0	8	3

increases the PODs for RA by 1% and FZRA by 5% relative to SBC-MMP (Table 2). It also subtly decreases the FAR for these categories. Taking the additional step of removing soundings where the observed precipitation type is inconsistent with the sounding (see section 2c) substantially increases the PODs to between 72% and 84% regardless of Z_H (Fig. 1b; see line marked SBC-NL*). Although making these assumptions is not a pure one-to-one comparison, this approach gives the best direct comparison with previous work.

b. Capability to diagnose the phase aloft

A method to indicate the phase aloft is necessary to meet the FAA requirements. This can be done by assigning the bin phases in the vertical as well as across the PSD. An example of this at Albany, New York, at 0000 UTC 26 January 2020 is provided in Figs. 4a–c. This profile has a deep warm layer at the surface that results in a diagnosis of RA. Aloft is a second warm layer that caps an elevated subfreezing layer wherein only partial melting and refreezing occur (Fig. 4b). The vertical phase diagnosis shows that the elevated subfreezing layer is characterized by FZDZ, FZRA, and FZRAPL. An obvious solution

to meet the requirements for three dimensionality is to provide the altitude of these sorts of layers as an additional grid. However, some profiles are quite complex, such as that at Wilmington, Ohio, at 1200 UTC 20 February 2019 (Figs. 4d–f). This sounding has two elevated subfreezing layers with different phase compositions and depths. The higher layer is comparatively shallow and has only FZDZ and PL while the lower one is deeper and has both FZDZ and FZRA but no PL. Distilling this level of detail into simple, quickly interrogated graphics is challenging.

A viable approach that conveys the presence of FZRA/FZDZ aloft is to output the most dangerous hydrometeor phase in the lowest 12 000 ft (i.e., the top of the TAS) as a single two-dimensional grid. This allows forecasters to quickly assess whether a threat exists and focus their attention on vertical profiles only in those places. Herein we assume FZRA is the most hazardous phase followed, in order, by FZDZ, PL, SN, RA, and then DZ. This sorting matches the hazard prioritization used by the FAA (FAA 2015). The resulting product is referred to as SBC-LA (low altitude; Table 1). The reader will note that mixes are not included in SBC-LA. This is by deliberate choice in order to simplify the logic and interpretation.
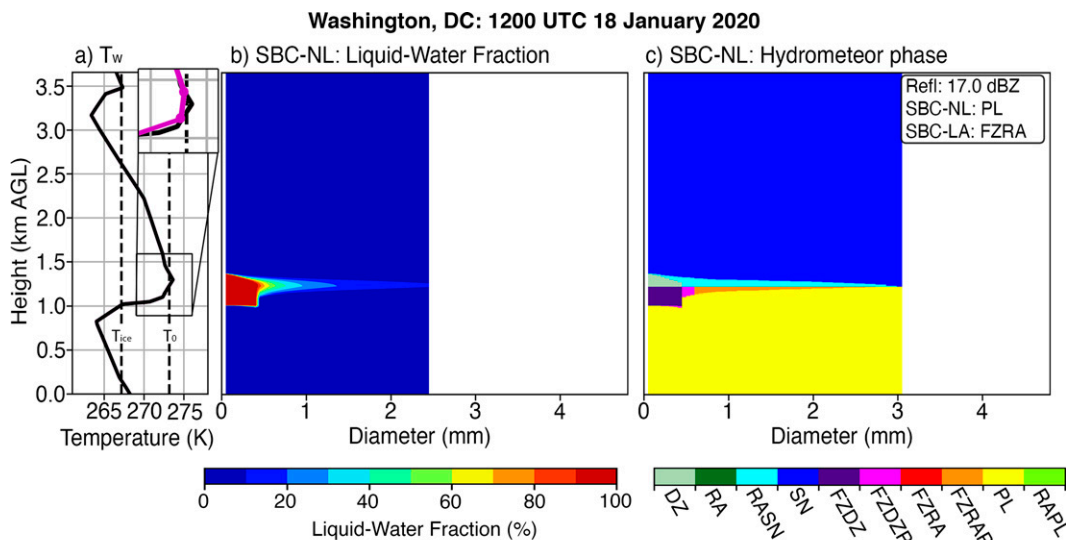

FIG. 5. (a) The T_w profile, and the SBC-NL diagnosis of (b) LWF and (c) hydrometeor phase. The inset in (a) shows T_w at full resolution (black) and interpolated to 25 hPa (magenta). Relevant diagnostics are included in the inset of (c).
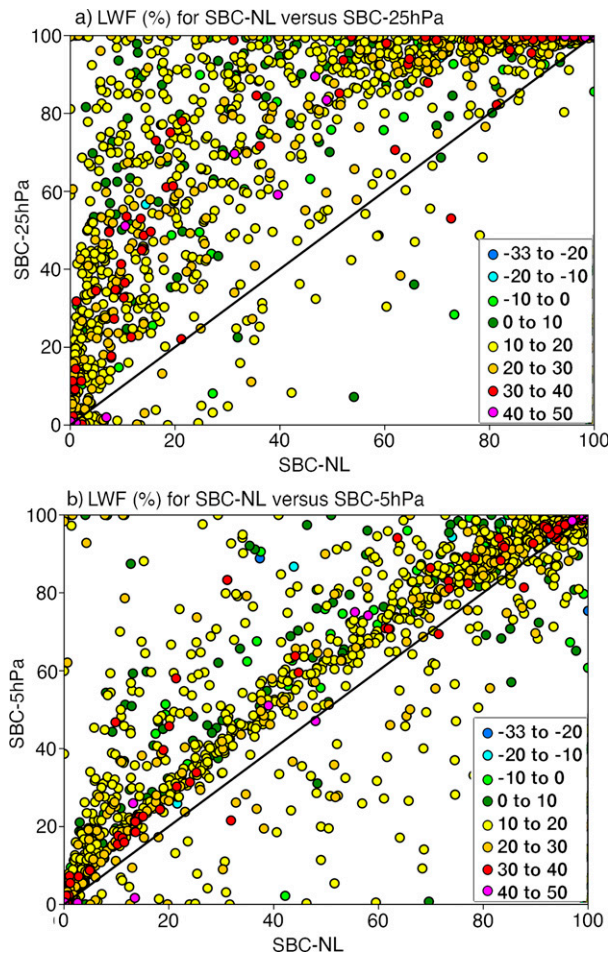
FIG. 6. Scatterplots of LWF for SBC-MMP vs (a) SBC-25hPa and (b) SBC-5hPa. Output is color coded according to the observed Z_H as indicated in the insets.

TABLE 6. As in Table 3, but comparing SBC-MMP with SBC-25hPa and SBC-5hPa.

	SBC-MMP					
	RA	RASN	FZRA	PL	FZRAPL	RAPL
SBC-25hPa:						
RA	**99**	73	0	2	0	44
RASN	1	**27**	0	2	0	17
FZRA	0	0	**100**	7	16	0
PL	0	0	0	**73**	10	0
FZRAPL	0	0	0	1	**59**	0
RAPL	0	0	0	15	15	**39**
SBC-5hPa:						
RA	**99**	28	0	2	0	26
RASN	1	**72**	0	1	0	20
FZRA	0	0	**96**	7	0	0
PL	0	0	4	**74**	8	0
FZRAPL	0	0	0	1	**61**	0
RAPL	0	0	0	15	31	**54**

Although the SBC-LA diagnoses cannot be validated because of a lack of robust aboveground observations, comparison with the surface phase diagnoses from SBC-NL is revealing (Table 5). Some categories are not different (e.g., SN, FZRA, FZDZ) or are changed to what one would expect (e.g., PL, and all mixes). Of interest for aviation applications, though, is that about 35% of all RA and DZ profiles are classified as FZRA or FZDZ by SBC-LA. Such a finding is consistent with previous research (Bernstein et al. 1998) and underscores the importance of an aboveground diagnosis. This fraction, of course, is only representative of the near-0°C environment. Warmer environments are unlikely to have such a high rate of FZRA/FZDZ aloft.

4. Applying the SBC to NWP output

a. Sensitivity to vertical resolution

An important consideration for CONUS-wide implementation is the transition to NWP analyses, which typically have a lower vertical resolution than observed soundings. To quantify the effects of this, all of the soundings are linearly interpolated

to a grid spacing of 25 hPa and are then applied to the SBC. The choice of 25 hPa is based on the resolution publicly disseminated NWP output by the National Weather Service in pressure coordinates. This output is referred to as SBC-25hPa (Table 1). Interpolating to a coarser resolution causes shallow melting and/or refreezing layers to go unresolved in 6% of the soundings. One such example is at Washington, DC, at 1200 UTC 18 January 2020. The observed sounding has a very-shallow elevated warm layer (Fig. 5a) that is sufficient for complete melting of hydrometeors less than 0.4 mm and partial melting of larger ones (Fig. 5b). When applied to SBC-NL, this results in a classification of PL below about 1 km AGL (Fig. 5c). The elevated melting layer is not resolved at 25 hPa (Fig. 5a; inset) leading to a completely subfreezing profile and a diagnosis of SN throughout the vertical column (not shown).

More often, decreasing the resolution only changes the depth and mean temperature of melting and refreezing layers, which usually results in a much higher integrated LWF for most profiles, independent of Z_H (Fig. 6a). This acts to increase both the POD and FAR relative to SBC-NL (Table 2) because the mean layer temperatures are usually warmer as the vertical resolution is decreased. Differences in LWF can be mitigated by interpolating to a higher resolution. This is demonstrated by linearly interpolating all of the soundings from 25 to 5 hPa. We refer to this output as SBC-5hPa (Table 1). The high-LWF bias is greatly decreased in SBC-5hPa (Fig. 6b) with RASN profiles being the most benefitted. These soundings have an increased in the rate of agreement from 27% to 72%; Table 6). Diagnoses of RAPL are also improved. However, profiles with partial melting and refreezing are not as benefitted by the reinterpolation: Rates of agreement for PL and FZRAPL are only increased by 1% and 2%, respectively.

SBC-25hPa and SBC-5hPa are included in Table 2 and show that SBC-5hPa has closer agreement to SBC-NL*. However, the FAR for RA is considerably increased, suggesting even with the interpolation to 5 hPa, there is still a warm bias. When the correction for RA/DZ and quality control of soundings is applied, SBC-5hPa's POD distribution as a function of Z_H shows good agreement with SBC-NL*.
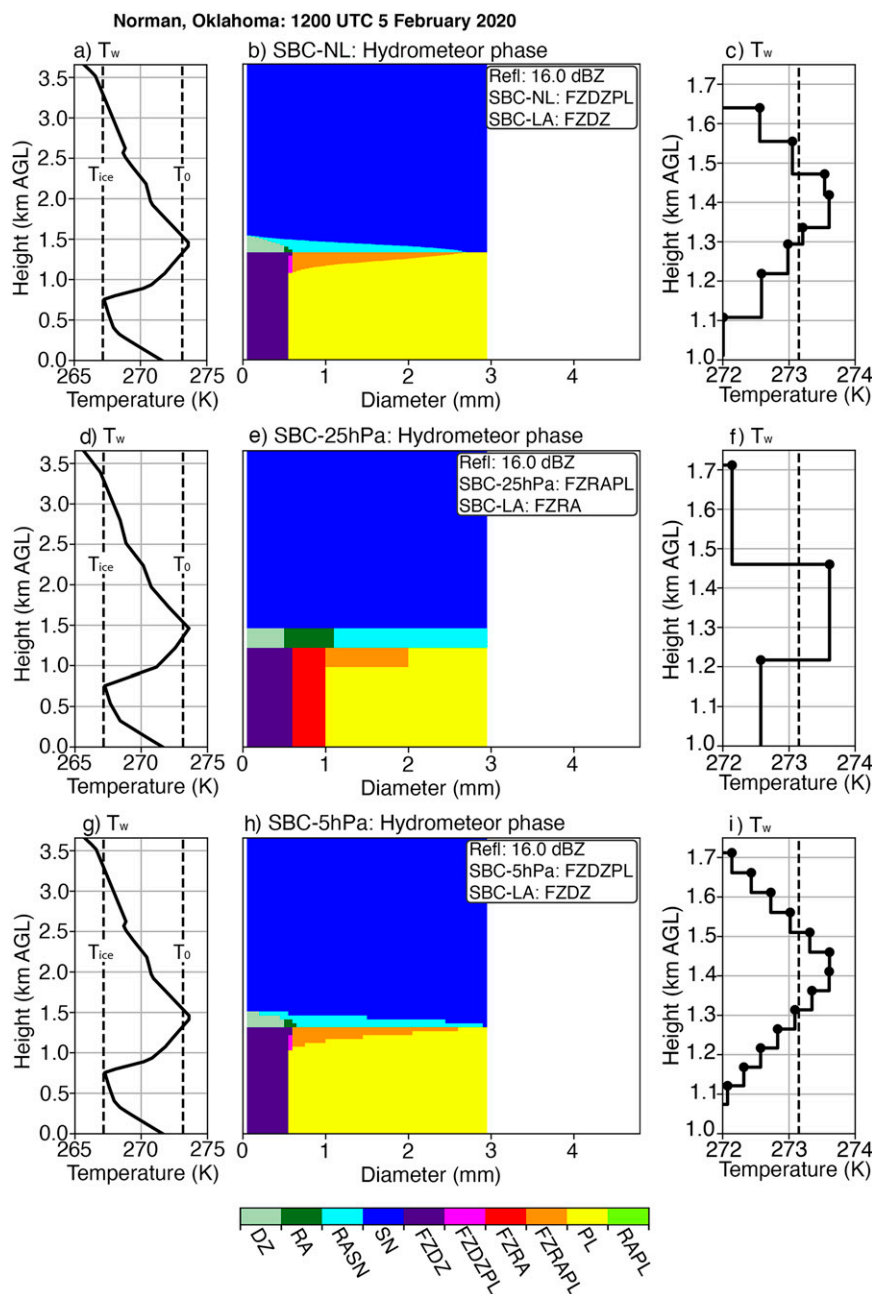
FIG. 7. (a),(d),(g) Vertical profiles of T_w; hydrometeor phase diagnosis from (b) SBC-NL, (e) SBC-25hPa, and (h) SBC-5hPa; (c),(f),(i) zoomed-in views of T_w near the melting layer at Norman at 1200 UTC 5 Feb 2020.

Interpolating to 5 hPa can add decision support value for profiles with partial melting/refreezing. This is highlighted using the 1200 UTC 5 February 2020 Norman, Oklahoma, sounding (Fig. 7). This profile has a very shallow elevated warm layer that only allows for particles smaller than 0.5 mm to completely melt in SBC-NL (Figs. 7a,b). A zoomed-in view of the melting layer in this sounding shows that it is less than 200 m deep (Fig. 7c). Because the surface-based subfreezing layer is warmer than T_{ice}, these particles do not refreeze

before reaching the surface, leading to FZDZ in the lowest 12 000 ft. Larger particles are categorized as PL. The elevated warm layer is resolved at 25 hPa (Fig. 7d), but the maximum particle size that completely melts is about 1 mm, resulting in some FZRA in the lowest 12 000 ft (Fig. 7e). With this vertical resolution, the melting layer is about 250 m deep (Fig. 7f). This change in diagnosis could force a diversion for certain aircraft. SBC-5hPa has better agreement with SBC-NL, producing only FZDZ and PL in the lowest 12 000 ft (Figs. 7g,h)
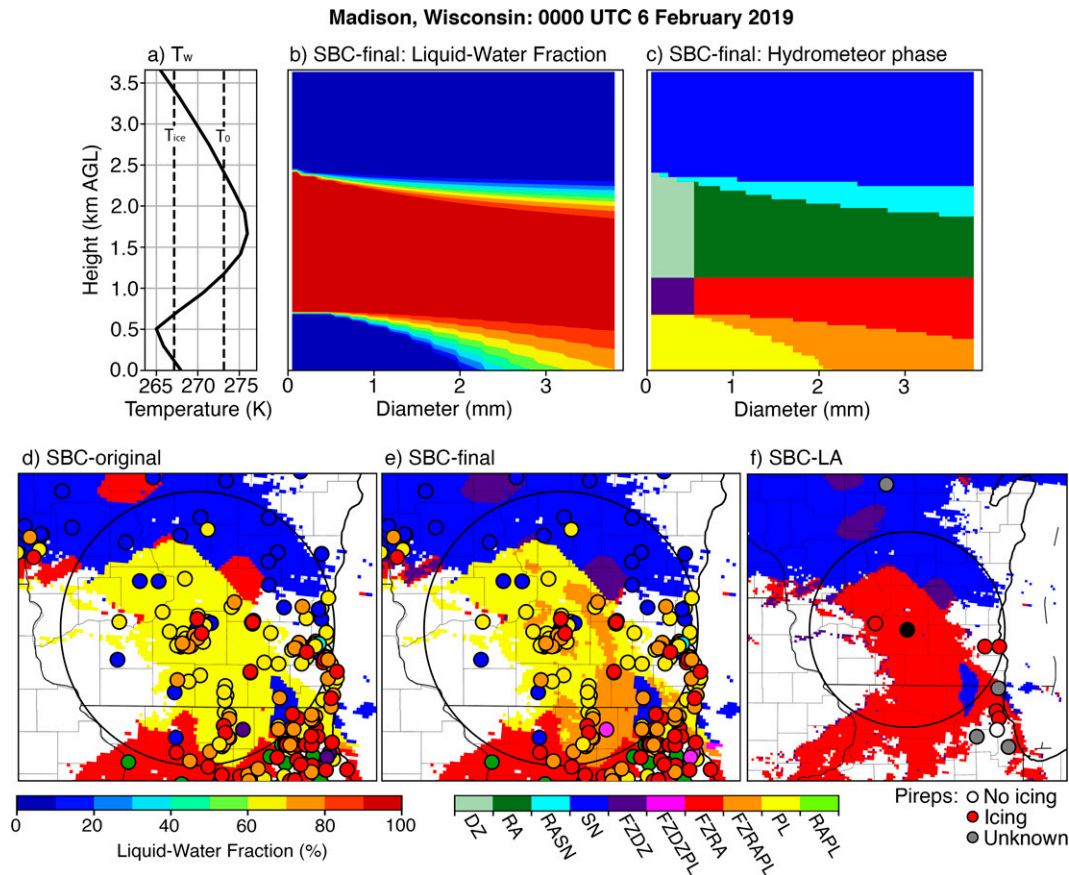
FIG. 8. HRRR-analyzed vertical profiles of (a) T_w, (b) LWF, and (c) hydrometeor phase at Madison, and plan views of the hydrometeor phase for (d) SBC-original, (e) SBC-final, and (f) SBC-LA. The location of the airport is provided in (f). The boundary of the TAS is provided in (d)–(f). Surface observations from ASOS and mPING are overlaid in (d) and (e).

and a melting layer that is closer in depth to the observations (196 m; Fig. 7i).

b. Application of the SBC-MMP to NWP output

We now attempt to apply the SBC to the High-Resolution Rapid Refresh (HRRR; Brown et al. 2011) analyses, which are produced hourly and have horizontal and vertical grid spacings of 3 km and 25 hPa, respectively. The version of the SBC used in this section includes the MMP, NL, LA, and 5 hPa upgrades described above and is referred to as SBC-final. These analyses are compared with surrounding ASOS and meteorological Phenomena Identification Near the Ground observations (mPING; Elmore et al. 2014). Radar reflectivity comes from the Multi-Radar Multi-Sensor (MRMS; Smith et al. 2016) system's base-reflectivity mosaic. The frozen versus liquid discrimination is made using the height of the lowest tilt relative to the 0°C isotherm from the HRRR model.

The first example occurs at Madison, Wisconsin, at 0000 UTC 6 February 2019. The T_w profile has an elevated warm layer that causes complete melting of all particles aloft (Figs. 8a,b). There is some partial and complete refreezing before particles reach the ground, depending on their diameter. There is a 500-m-deep

layer of FZRA/FZDZ at about 700 m AGL (Fig. 8c). The resulting diagnoses are PL in SBC-original as its maximum particle size is 1.85 mm, FZRAPL in SBC-final, and FZRA in SBC-LA. Plan views of the hydrometeor phase for the entire TAS (denoted by the circular areas in Figs. 8d–f) show SBC-original produces mostly PL surrounding the airport with SN to the north and FZRA to the south (Fig. 8d). The region of SN agrees with most observations in that area, but elsewhere the observations suggest a heterogeneous mix of PL, FZRAPL, FZRA, and SN. The SBC-original diagnosis is not reflective of that mix. The SBC-final diagnosis FZRAPL immediately over the airport and to the east and southeast (Fig. 8e) better agrees with the observations, but it is not a one-to-one correspondence either. A one-to-one agreement is extremely unlikely given that the observed variability exceeds what can be resolved by the HRRR model (Reeves 2016) and the fact that uncertainty in model profiles affects algorithm performance (Wandishin et al. 2005; Reeves et al. 2014).

SBC-LA shows FZRA is present at some level below 12 000 ft at every point immediately surrounding the airport and to its south (Fig. 8f). A qualitative validation of the SBC-LA output is provided using pilot reports (PIREPs) collected
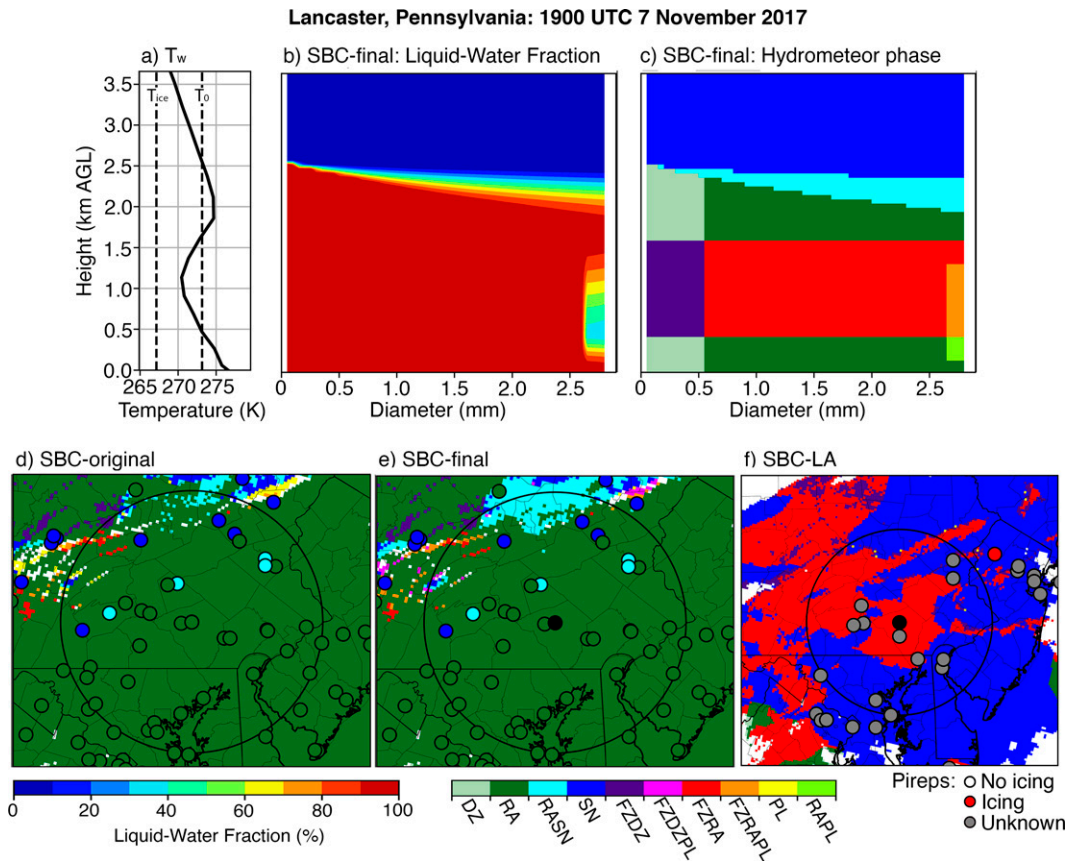
FIG. 9. As in Fig. 8, but at Lancaster.

during the 2-h window surrounding the analysis time and that are below 12 000 ft AGL. There are only few reports within this TAS as PIREPs are less common during ascent and descent. It is also likely that planes are avoiding this area due to the FZRA. Hence a slightly larger area is shown to include more observations. There are five icing reports in the domain that are in or near areas identified as FZRA by SBC-LA. There is one report of no icing in an area of nonprecipitation. Other reports did not include icing information (a lack of icing information does not imply there is no icing or vice versa; P. Suffern 2021, personal communication).

A different scenario is provided in Lancaster, Pennsylvania, at 1900 UTC 7 November 2017. This profile is more complex than the previous one, having three crossings of the 0°C isotherm (Fig. 9a). The surface layer is sufficiently warm and deep for complete melting of all hydrometeors resulting in RA/DZ at the surface across the entire PSD (Figs. 9b,c). There is a deep elevated subfreezing layer that results in FZDZ, FZRA, and FZRAPL aloft. Plan views lend additional insight. Both SBC-original and SBC-final suggest mostly RA in this TAS, which agree with the majority of surface observations (Figs. 9d,e). (Observations of SN and RASN in the complex terrain of the Allegheny Mountains are likely due to local terrain influences that are not fully captured by the HRRR model.) SBC-LA indicates FZRA immediately over this airport and to the west (Fig. 9f). Unfortunately, none

of the PIREPs surrounding this airport include icing information. But the limited amount of air traffic in areas of FZRA suggests avoidance possibly because of icing concerns.

A final example from Grand Rapids, Michigan, at 1800 UTC 18 January 2020 shows a third scenario. This example highlights a simple profile with only one crossing of the 0°C isotherm (Fig. 10a). Particles with diameters less than 1.7 mm completely melt in the surface layer, resulting in a diagnosis of RA, while larger particles only partially melt, resulting in a diagnosis of RASN (Figs. 10b,c). Because its D_{max} is smaller, SBC-original indicates mostly RA surrounding the airport with RASN and SN to the north (Fig. 10d). Surface observations suggest SN and RASN immediately surrounding the airport. SBC-final more accurately captures the southward extent of RASN (Fig. 10e). Though RASN does not necessarily impact icing, in some situations a change in phase can impact hold over times and the type/quantity of deicing chemicals that are required. SBC-LA suggests the most hazardous form in this TAS is SN (Fig. 10f). There are very few PIREPs in the vicinity of this TAS—only a handful in an area of nonprecipitating cloud (i.e., no radar returns) to the west of the TAS and four reports to the east that did not include icing information.

In summary, though the differences between SBC-original and SBC-final may appear minor for most applications, the above analyses demonstrate they can influence decisions and affect air traffic. Unfortunately, the number of PIREPs in

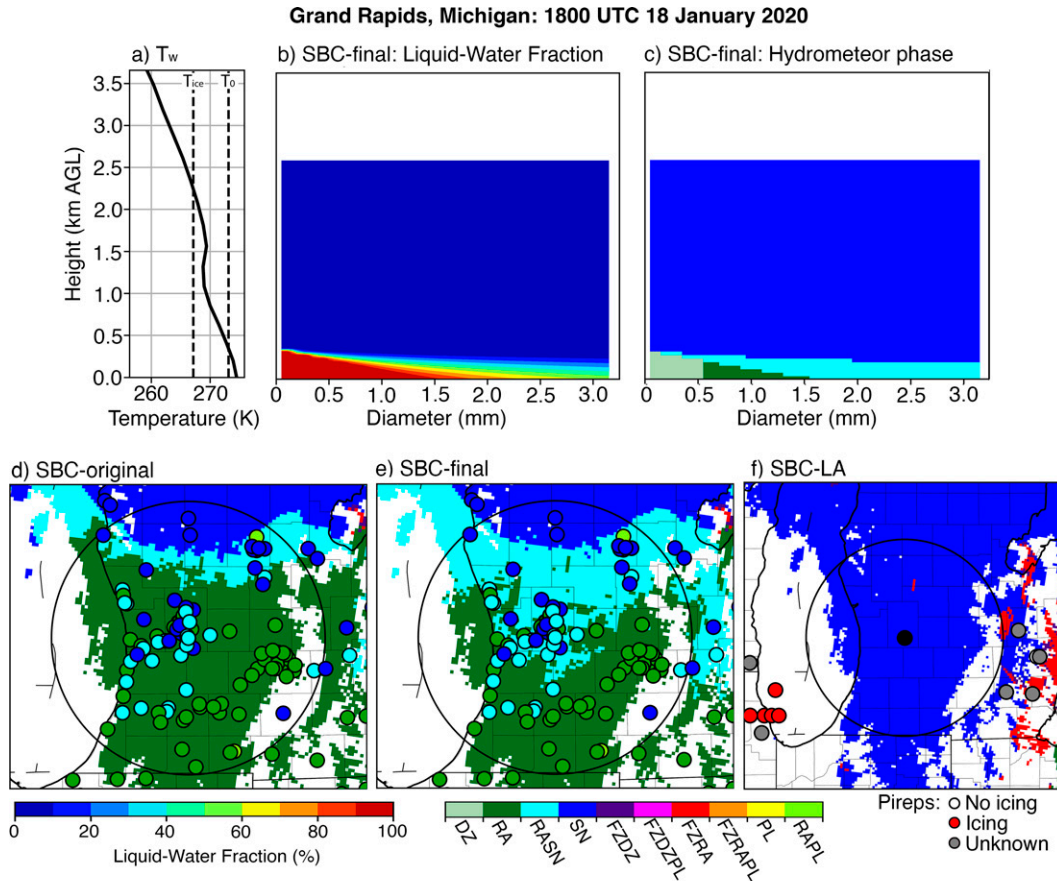**Grand Rapids, Michigan: 1800 UTC 18 January 2020**

FIG. 10. As in Fig. 8, but at Grand Rapids.

TASs is somewhat limited to give robust guidance on the performance of SBC-LA.

5. Conclusions

New regulations emerging from the FAA require explicit discrimination between FZDZ, FZRA, and other forms of precipitation that may result in aircraft icing. This diagnosis is needed throughout a three-dimensional volume surrounding all commercial airports in the United States. Herein, a novel hydrometeor-phase algorithm, the spectral bin classifier (SBC), is adapted to add capabilities to meet these demands.

Two upgrades required to discriminate between FZRA and FZDZ are evaluated. The first is the addition of a dynamic PSD that is achieved by using a simple reflectivity-based Marshall–Palmer distribution. This approach shows good improvement over the static PSD, with probability of detection increasing by ~12%. It has the additional advantage of being compatible with mosaicked reflectivity, which greatly aids in the computational efficiency of the algorithm and its viability for near-term transition into operations. The second upgrade is a change in the logic used to declare the precipitation type. This change exploits the dynamic-PSD capability by declaring the phase in individual bins as opposed to using the integrated LWF. This allows for

DZ and FZDZ to be diagnosed. While this has obvious benefits for meeting the FAA needs, ambiguities in the ASOS discrimination between RA and DZ as well as between FZRA and FZDZ cause the PODs for this version of the SBC to worsen relative to the original version of the algorithm. So, some effort to better distinguish these types of observations is merited going forward.

A capability to extract the aboveground phase to give a low-altitude diagnosis is also introduced. Given how complex the vertical profile of hydrometeor phase can be, a simple approach that provides the most-hazardous phase in the lowest 12 000 ft AGL is advocated for quick-glance decision making. This move away from a surface-only diagnosis has some clear benefits for the aviation sector, showing that about 35% of all RA and DZ profiles in this study have an elevated layer of FZRA or FZDZ. While this fraction is only representative of the near-0°C environment, it is still considerable and highlights the importance of knowing the phase aloft.

Last, the effects of transitioning from observed to NWP soundings is considered as degraded performance is noted as the vertical resolution is decreased. Some layers critical to the phase evolution of falling hydrometeors cannot be resolved at 25 hPa, but a larger problem is subtle changes to the rates of melting and refreezing that lead to consequential changes in

the LWF at the surface. This is mitigated by interpolating from 25 to 5 hPa before applying the profiles to the SBC. The resulting PODs are improved using this approach.

Several potential points of departure from this research are worthy of note. One is the possible importance of secondary ice multiplication for low-Z_H profiles, which appears to shift observations to SN for soundings that have elevated warm layers. This microphysical impact is not accounted for in the SBC and, therefore, could result in misdiagnoses. The frequency and impact of this on decision making have yet to be quantified. While using a Marshall–Palmer-type PSD improves algorithm performance, a reflectivity-dependent approach has some drawbacks. It is not as sophisticated and is potentially less accurate than methods that use dual-polarized radar observations. But these methods are still in their infancy and may be several years away from real-time implementation. Of greater consequence is the fact that some shallow and weak precipitation systems are overshot by neighboring radars or are removed during quality control (Reeves and Waters 2019). Methods to provide a diagnosis in the absence of radar observations must be devised. Despite these unanswered questions/issues, the advancements made herein still stand as an important forward step toward meeting emerging needs and providing enhanced decision support for aviation.

Data availability statement. ASOS observations are archived and accessible via https://mesowest.utah.edu. mPING observations are archived and accessible via https://mping.ou.edu. Sounding data are archived and accessible via https://weather.uwyo.edu/upperair/sounding.html. HRRR analyses are archived and accessible via https://home.chpc.utah.edu/~u055130/Brian_Blaylock/cgi-bin/hrrr_download.cgi. Because of their proprietary nature, data created as a part of this research and the MRMS data used in this study cannot be made openly available.

REFERENCES

Benjamin, S. G., J. M. Brown, and T. G. Smirnova, 2016: Explicit precipitation-type diagnosis from a model using a mixed-phase bulk cloud–precipitation microphysics parameterization. *Wea. Forecasting*, **31**, 609–619, https://doi.org/10.1175/WAF-D-15-0136.1.

Bernstein, B. C., 2000: Regional and local influences on freezing drizzle, freezing rain, and ice pellet events. *Wea. Forecasting*, **15**, 485–508, https://doi.org/10.1175/1520-0434(2000)015<0485:RALIOF>2.0.CO;2.

——, T. A. Omeron, M. K. Politovich, and F. McDonough, 1998: Surface weather features associated with freezing precipitation and severe in-flight aircraft icing. *Atmos. Res.*, **46**, 57–73, https://doi.org/10.1016/S0169-8095(97)00051-3.

——, F. McDonough, M. K. Politovich, B. G. Brown, T. P. Ratvasky, D. R. Miller, C. A. Wolff, and G. Cunning, 2005: Current icing potential: Algorithm description and comparison with aircraft observations. *J. Appl. Meteor. Climatol.*, **44**, 969–986, https://doi.org/10.1175/JAM2246.1.

Blaylock, B., J. Horel, and S. Liston, 2017: Cloud archival and data mining of High Resolution Rapid Refresh forecast model output. *Comput. Geosci.*, **109**, 43–50, https://doi.org/10.1016/j.cageo.2017.08.005.

Bourgouin, P., 2000: A method to determine precipitation types. *Wea. Forecasting*, **15**, 583–592, https://doi.org/10.1175/1520-0434(2000)015<0583:AMTDPT>2.0.CO;2.

Brown, J. M., and Coauthors, 2011: Improvement and testing of WRF physics options for application to Rapid Refresh and High Resolution Rapid Refresh. *14th Conf. on Mesoscale Processes/15th Conf. on Aviation, Range, and Aerospace Meteorology*, Los Angeles, CA, Amer. Meteor. Soc., 5.5, https://ams.confex.com/ams/14Meso15ARAM/webprogram/Paper191234.html.

Bukovčić, P., A. Ryzhkov, D. Zrnic, and G. Zhang, 2018: Polarimetric radar relations for quantification of snow based on disdrometer data. *J. Appl. Meteor. Climatol.*, **57**, 103–120, https://doi.org/10.1175/JAMC-D-17-0090.1.

——, ——, and ——, 2020: Polarimetric relations for snow estimation – Radar verification. *J. Appl. Meteor. Climatol.*, **59**, 991–1009, https://doi.org/10.1175/JAMC-D-19-0140.1.

Cao, Q., G. Zhang, T. Schuur, A. Ryzhkov, E. Brandes, and K. Ikeda, 2006: Characterization of rain microphysics based on disdrometer and polarimetric radar observations. *2006 IEEE Int. Symp. on Geoscience and Remote Sensing*, Institute of Electrical and Electronics Engineers, 523–528.

——, ——, E. Brandes, T. Schuur, A. Ryzhkov, and K. Ikeda, 2008: Analysis of video disdrometer and polarimetric radar data to characterize rain microphysics in Oklahoma. *J. Appl. Meteor. Climatol.*, **47**, 2238–2255, https://doi.org/10.1175/2008JAMC1732.1.

Cho, J. Y. N., 2010: OEP terminal and CONUS weather radar coverage gap identification analysis for NextGen. MIT Lincoln Laboratory Project Rep. ATC-369, 93 pp., https://www.ll.mit.edu/sites/default/files/publication/doc/2018-09/Cho_2010_ATC-369_WW-20740.pdf.

Cober, S. G., and G. A. Isaac, 2012: Characterization of aircraft icing environments with supercooled large drops for application to commercial aircraft certification. *J. Appl. Meteor. Climatol.*, **51**, 265–284, https://doi.org/10.1175/JAMC-D-11-022.1.

Elmore, K. L., Z. L. Flamig, V. Lakshmanan, B. Kaney, V. Farmer, H. D. Reeves, and L. P. Rothfusz, 2014: MPING: Crowd-sourcing weather reports for research. *Bull. Amer. Meteor. Soc.*, **95**, 1335–1342, https://doi.org/10.1175/BAMS-D-13-00014.1.

——, H. M. Grams, D. Apps, and H. D. Reeves, 2015: Verifying forecast precipitation type with mPING. *Wea. Forecasting*, **30**, 656–667, https://doi.org/10.1175/WAF-D-14-00068.1.

FAA, 2009: Data and analysis for the development of an engineering standard for supercooled large drop conditions. Federal Aviation Administration Rep., 77 pp.

——, 2015: Airplane and engine certification requirements in supercooled large drop, mixed phase, and ice crystal icing conditions; final rule. Parts 25 and 33, Aeronautics and Space,

U.S. Code of Federal Regulations, National Archives and Records Administration, 34 pp.

Giangrande, S. E., A. V. Ryzhkov, and J. Krause, 2005: Automatic detection of the melting layer with a polarimetric prototype of the WSR-88D radar. *32nd Conf. on Radar Meteorology*, Albuquerque, NM, Amer. Meteor. Soc., 11R.2, https://ams.confex.com/ams/pdfpapers/95894.pdf.

Gunn, K., and J. S. Marshall, 1958: The distribution with size of aggregate snowflakes. *J. Meteor.*, **15**, 452–461, https://doi.org/10.1175/1520-0469(1958)015<0452:TDWSOA>2.0.CO;2.

Hallowell, R. G., M. F. Donovan, D. J. Smalley, and B. J. Bennett, 2013: Icing hazard detection with NEXRAD IHL. *36th Conf. on Radar Meteorology*, Breckenridge, CO, Amer. Meteor. Soc., 12.263, https://ams.confex.com/ams/36Radar/webprogram/Manuscript/Paper228656/Hallowell_36RADAR_AMS.pdf.

Heymsfield, A. J., A. Bansemer, P. R. Field, S. L. Durden, J. L. Stith, J. E. Dye, W. Hall, and C. A. Grainger, 2002: Observations and parameterizations of particle size distributions in deep tropical cirrus and stratiform precipitating clouds: Results from in situ observations in TRMM field campaigns. *J. Atmos. Sci.*, **59**, 3457–3491, https://doi.org/10.1175/1520-0469(2002)059<3457:OAPOPS>2.0.CO;2.

——, C. G. Schmitt, A. R. Bansemer, and C. H. Twohy, 2010: Improved representation of ice particle masses based on observations in natural clouds. *J. Atmos. Sci.*, **67**, 3303–3318, https://doi.org/10.1175/2010JAS3507.1.

Ikeda, K., M. Steiner, J. Pinto, and C. Alexander, 2013: Evaluation of cold-season precipitation forecasts generated by the hourly updating High-Resolution Rapid Refresh model. *Wea. Forecasting*, **28**, 921–939, https://doi.org/10.1175/WAF-D-12-00085.1.

Kumjian, M. R., S. M. Ganson, and A. V. Ryzhkov, 2012: Freezing of raindrops in deep convective updrafts: A microphysical and polarimetric model. *J. Atmos. Sci.*, **69**, 3471–3490, https://doi.org/10.1175/JAS-D-12-067.1.

Lauber, A., A. Kiselev, T. Pander, P. Handmanm, and T. Leisner, 2018: Secondary ice formation during freezing of levitated droplets. *J. Atmos. Sci.*, **75**, 2815–2826, https://doi.org/10.1175/JAS-D-18-0052.1.

Mahale, V. N., G. Zhang, M. Xue, J. Gao, and H. D. Reeves, 2019: Variational retrieval of rain microphysics and related parameters from polarimetric radar data with a parameterized operator. *J. Atmos. Oceanic Technol.*, **36**, 2483–2500, https://doi.org/10.1175/JTECH-D-18-0212.1.

Manikin, G. S., 2005: An overview of precipitation type forecasting using NAM and SREF data. *24th Conf. on Broadcast Meteorology/21st Conf. on Weather Analysis and Forecasting/17th Conf. on Numerical Weather Prediction*, Washington, DC, Amer. Meteor. Soc., 8A.6, https://ams.confex.com/ams/pdfpapers/94838.pdf.

——, K. F. Brill, and B. Ferrier, 2004: An eta model precipitation type mini-ensemble for winter weather forecasting. *20th Conf. on Weather Analysis and Forecasting/16th Conf. on Numerical Weather Prediction*, Seattle, WA, Amer. Meteor. Soc., 23.1, https://ams.confex.com/ams/pdfpapers/73517.pdf.

Marshall, J. S., and W. M. Palmer, 1948: The distribution of raindrops with size. *J. Meteor.*, **5**, 165–166, https://doi.org/10.1175/1520-0469(1948)005<0165:TDORWS>2.0.CO;2.

NOAA, 1998: Automated Surface Observing System: User's guide. National Oceanic and Atmospheric Administration Doc., 61 pp., https://www.weather.gov/media/asos/aum-toc.pdf.

Park, H. S., A. V. Ryzhkov, D. S. Zrnić, and K.-E. Kim, 2009: The hydrometeor classification algorithm for the polarimetric WSR-88D: Description and application to an MCS. *Wea. Forecasting*, **24**, 730–748, https://doi.org/10.1175/2008WAF2222205.1.

Phillips, V. T., S. Patade, J. Gutierrez, and A. Bansemer, 2018: Secondary ice production by fragmentation of freezing drops: Formulation and theory. *J. Atmos. Sci.*, **75**, 3031–3070, https://doi.org/10.1175/JAS-D-17-0190.1.

Plummer, D. M., S. Göke, R. M. Rauber, and L. Di Girolamo, 2010: Discrimination of mixed- versus ice-phase clouds using dual-polarization radar with application to detection of aircraft icing regions. *J. Appl. Meteor. Climatol.*, **49**, 920–936, https://doi.org/10.1175/2009JAMC2267.1.

Ramer, J., 1993: An empirical technique for diagnosing precipitation type from model output. *Fifth Int. Conf. on Aviation Weather Systems*, Vienna, VA, Amer. Meteor. Soc., 227–230.

Reeves, H. D., 2016: The uncertainty of precipitation-type observations and its effect on the validation of forecast precipitation type. *Wea. Forecasting*, **31**, 1961–1971, https://doi.org/10.1175/WAF-D-16-0068.1.

——, and J. Waters, 2019: Dual-polarized radar coverage in terminal airspaces and its effect on interpretation of winter weather signatures: Current capabilities and future recommendations. *J. Appl. Meteor. Climatol.*, **58**, 165–183, https://doi.org/10.1175/JAMC-D-18-0123.1.

——, K. L. Elmore, A. Ryzhkov, T. Schuur, and J. Krause, 2014: Sources of uncertainty in precipitation-type forecasting. *Wea. Forecasting*, **29**, 936–953, https://doi.org/10.1175/WAF-D-14-00007.1.

——, A. V. Ryzhkov, and J. Krause, 2016: Discrimination between winter precipitation types based on spectral-bin microphysical modeling. *J. Appl. Meteor. Climatol.*, **55**, 1747–1761, https://doi.org/10.1175/JAMC-D-16-0044.1.

Ryzhkov, A. V., 2007: The impact of beam broadening on the quality of radar polarimetric data. *J. Atmos. Oceanic Technol.*, **24**, 729–744, https://doi.org/10.1175/JTECH2003.1.

——, T. J. Schuur, D. W. Burgess, P. L. Heinselman, S. E. Giangrande, and D. S. Zrnic, 2005: The Joint Polarization Experiment: Polarimetric rainfall measurements and hydrometeor classification. *Bull. Amer. Meteor. Soc.*, **86**, 809–824, https://doi.org/10.1175/BAMS-86-6-809.

Schuur, T. J., A. V. Ryzhkov, and D. R. Clabo, 2005: Climatological analysis of DSDs in Oklahoma as revealed by 2D-video disdrometer and polarimetric WSR-88D radar. *32nd Conf. on Radar Meteorology*, Albuquerque, NM, Amer. Meteor. Soc., 15R.4, https://ams.confex.com/ams/pdfpapers/95995.pdf.

Seidel, D. J., B. Sun, M. Petty, and A. Reale, 2011: Global radiosonde balloon drift statistics. *J. Geophys. Res.*, **116**, D07102, https://doi.org/10.1029/2010JD014891.

Sekhon, R. S., and R. C. Srivastava, 1970: Snow spectra and radar reflectivity. *J. Atmos. Sci.*, **27**, 299–307, https://doi.org/10.1175/1520-0469(1970)027<0299:SSSARR>2.0.CO;2.

Serke, D., S. Ellis, J. Hubbert, D. Albo, C. Johnston, C. Coy, D. Adriaanson, and M. Politovich, 2013: In-flight icing hazard detection with dual and single-polarimetric moments from operational NEXRADs. *36th Conf. on Radar Meteorology*, Breckenridge, CO, Amer. Meteor. Soc., 15A.4, https://ams.confex.com/ams/36Radar/webprogram/Manuscript/Paper228592/AMSRAD_2013_ex%20%281%29.pdf.

Smith, T. M., and Coauthors, 2016: Multi-Radar Multi-Sensor (MRMS) severe weather and aviation products: Initial operating

capabilities. *Bull. Amer. Meteor. Soc.*, **97**, 1617–1630, https://doi.org/10.1175/BAMS-D-14-00173.1.

Thompson, E. J., S. A. Rutledge, B. Dolan, V. Chandrasekar, and B. L. Cheong, 2014: A dual-polarization radar hydrometeor classification algorithm for winter precipitation. *J. Atmos. Oceanic Technol.*, **31**, 1457–1481, https://doi.org/10.1175/JTECH-D-13-00119.1.

Thompson, G., R. M. Rasmussen, and K. Manning, 2004: Explicit forecasts of winter precipitation using an improved bulk microphysics scheme. Part I: Description and sensitivity analysis. *Mon. Wea. Rev.*, **132**, 519–542, https://doi.org/10.1175/1520-0493(2004)132<0519:EFOWPU>2.0.CO;2.

Trömel, S., A. V. Ryzhkov, P. Zhang, and C. Simmer, 2014: Investigations of backscatter differential phase in the melting layer. *J. Appl. Meteor. Climatol.*, **53**, 2344–2359, https://doi.org/10.1175/JAMC-D-14-0050.1.

Waldvogel, A., 1974: The N_0 jump of raindrop spectra. *J. Atmos. Sci.*, **31**, 1067–1078, https://doi.org/10.1175/1520-0469(1974)031<1067:TJORS>2.0.CO;2.

Wandishin, M. S., M. E. Baldwin, S. L. Mullen, and J. V. Cortinas, 2005: Short-range ensemble forecasts of precipitation type. *Wea. Forecasting*, **20**, 609–626, https://doi.org/10.1175/WAF871.1.

Zhang, G., 2017: *Weather Radar Polarimetry*. CRC Press, 304 pp.

——, J. Sun, and E. A. Brandes, 2006: Improving parameterization of rain microphysics with disdrometer and radar observations. *J. Atmos. Sci.*, **63**, 1273–1290, https://doi.org/10.1175/JAS3680.1.

——, M. Xue, Q. Cao, and D. Dawson, 2008: Diagnosing the intercept parameter for exponential raindrop size distribution based on video disdrometer observations: Model development. *J. Appl. Meteor. Climatol.*, **47**, 2983–2992, https://doi.org/10.1175/2008JAMC1876.1.